

RESEARCH ARTICLE

10.1002/2017JB014237

Key Points:

- Work associated with breaking intact rock is the largest component of energy budget of fault growth
- Work optimization, a global growth criterion, does not require failure mode to be selected beforehand; failure can be in tension or shear
- Tensile failure at an angle to the parent fault releases energy for additional processes

Correspondence to:

E. H. Madden,
elizabeth.madden@imu.de

Citation:

Madden, E. H., M. L. Cooke, and J. McBeck (2017), Energy budget and propagation of faults via shearing and opening using work optimization, *J. Geophys. Res. Solid Earth*, 122, 6757–6772, doi:10.1002/2017JB014237.

Received 24 MAR 2017

Accepted 14 JUL 2017

Accepted article online 18 JUL 2017

Published online 3 AUG 2017

Energy budget and propagation of faults via shearing and opening using work optimization

Elizabeth H. Madden^{1,2} , Michele L. Cooke¹ , and Jessica McBeck^{1,3}
¹Department of Geosciences, University of Massachusetts Amherst, Amherst, Massachusetts, USA, ²Department of Earth and Environmental Sciences, Geophysics, Ludwig-Maximilians-Universität München, Munich, Germany, ³Physics of Geological Processes, Department of Physics, University of Oslo, Oslo, Norway

Abstract We present numerical models of faults propagating by work optimization in a homogeneous medium. These simulations allow quantification and comparison of the energy budgets of fault growth by shear versus tensile failure. The energy consumed by growth of a fault, W_{grow} , propagating by in-line shearing is 76% of the total energy associated with that growth, while 24% is spent on frictional work during propagation. W_{grow} for a fault propagating into intact rock by tensile failure, at an angle to the parent fault, consumes 60% of the work budget, while only 6% is consumed by frictional work associated with propagation. Following the conservation of energy, this leaves 34% of the energy budget available for other activities and suggests that out-of-plane propagation of faults in Earth's crust may release energy for other processes, such as permanent damage zone formation or rupture acceleration. Comparison of these estimates of W_{grow} with estimates of the critical energy release rate and earthquake fracture energy at several scales underscores their theoretical similarities and their dependence on stress drop.

1. Introduction

Faults reactivate in subsequent slip events and also extend and change their active shape over time. This behavior involves slip along preexisting surfaces as well as propagation into previously intact rock. Much effort has been applied to understanding failure mechanisms and the role of tensile versus shear failure in fault evolution at different scales [e.g., *Horii and Nemat-Nasser*, 1985; *Petit and Barquins*, 1988; *Crider and Peacock*, 2004; *Lunn et al.*, 2008; *Moir et al.*, 2010]. *Crider and Peacock* [2004] review numerous field observations of faulting in the shallow crust and highlight two styles of fault formation: the linkage of preexisting structures into throughgoing shear surfaces and the development of shear surfaces within preexisting shear zones. In both cases, they note that opening-mode structures play a critical role in early fault evolution. *Lunn et al.* [2008] model the spatial and temporal evolution of fault growth through linkage of damage zones near faults, while *Moir et al.* [2010] capture fault and damage zone development with models that simulate the linkage of preexisting joints. Shear failure through the coalescence of early tensile microfractures also is observed in laboratory experiments [e.g., *Horii and Nemat-Nasser*, 1985; *Petit and Barquins*, 1988; *Lockner et al.*, 1992]. These studies demonstrate the prevalence of both tensile and shear failure modes of fault evolution at many scales.

In order to model fault propagation, typically a choice about tensile versus shear failure must be made beforehand, so that one failure criterion can be invoked. However, work optimization [e.g., *Cooke and Madden*, 2014; *Yagupsky et al.*, 2014; *McBeck et al.*, 2016] provides a global scheme to determine the direction of propagation without having to select the failure mechanism a priori. This approach utilizes the concept of a balanced energy budget, first presented by *Griffith* [1921] for joints, and assumes that a system will evolve toward lower energy and higher efficiency. The numerical modeling tool *Growth by Optimization of Work* (GROW) [McBeck et al., 2016] takes advantage of this energy budget approach. While fault slip occurs when the stresses on a preexisting fault meet the fault strength and the failure of intact rock is permitted when the tensile or shear stress meets the tensile or shear strength of the intact rock, the propagation direction is that which achieves the highest mechanical efficiency for the entire system [McBeck et al., 2016]. Thus, GROW automates the growth of faults along paths that maximize the system's mechanical efficiency, allowing for propagation paths that are not restricted to growth solely by shear or opening-mode failure.

We compare modeled initial propagation angles, propagation paths, and coalescence patterns with those from laboratory experiments. We also compare the initial propagation angles determined by work

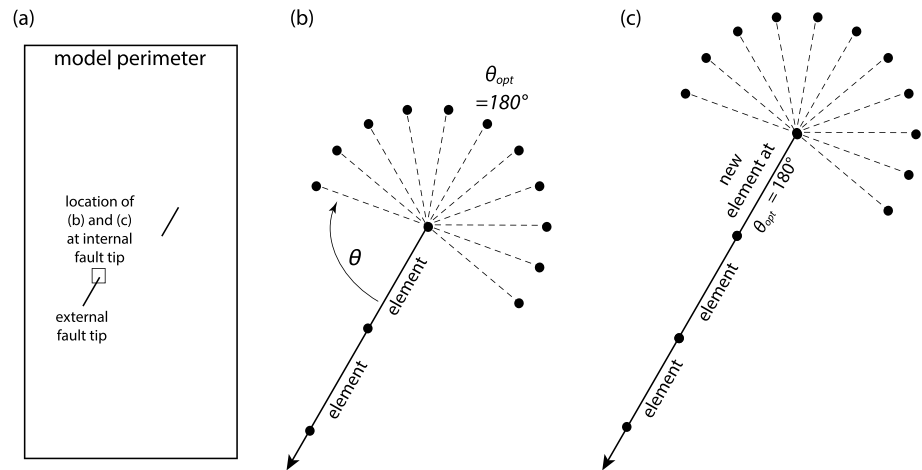


Figure 1. Schematic view of (a) model with perimeter and faults, (b) orientations of potential growth elements at one internal fault tip at angles θ , and (c) after one growth increment θ_{opt} , with new growth increment under evaluation. Arrows in Figures 1b and 1c indicate that fault continues. Process continues until either the fault intersects another surface or none of the potential growth elements fail.

optimization with those predicted by alternative failure criteria. These numerical simulations allow us to investigate the work budgets of propagating faults. We calculate the energy budget for the first increment of growth, including the work acting externally on the system, the internal strain energy density, the work against frictional resistance to slip, and the energy required for fault growth, W_{grow} . We discuss how the magnitude estimates of W_{grow} from these models compare with estimates of the critical energy release rate, G_c , from laboratory experiments and field observations of faults, and the fracture energy, G , from earthquake data and models.

2. Grow

GROW calls on the 2-D boundary element method program Fric2D to determine slip on preexisting surfaces and to evaluate failure in all potential propagation directions. GROW then selects the propagation direction of one or many growing faults based on work optimization [McBeck *et al.*, 2016]. Fric2D solves the quasi-static equations of motion for assigned boundary conditions, material properties, fault geometry, and fault friction [Cooke and Pollard, 1997]. Fric2D has been used extensively to study fault behavior, including damage development along frictional faults [Savage and Cooke, 2010], the energy of fault systems [Cooke and Murphy, 2004; Del Castello and Cooke, 2007; Cooke and Madden, 2014], and fault interactions [Cooke *et al.*, 2011; McBeck *et al.*, 2016].

Boundary conditions may be tractions, displacements, or a mixture of both applied on the model perimeters (Figure 1a). The material properties are isotropic and linear elastic. Any number of surfaces of discontinuity may be included within the model, such as the two faults shown in Figure 1a. The model perimeters and these fault surfaces are discretized into boundary elements, where the equations of motion are solved following the displacement discontinuity method [Crouch and Starfield, 1983]. The length of each fault element must be short enough to capture the concentrated stress field near the fault tip but long enough to exceed the zone of yielding due to singular stresses at the fault tip. In the verification available in the appendix, we show that an element length of 1% of the parent fault length is sufficient.

Shear failure along preexisting faults occurs when the shear stress magnitude, $|\tau|$, meets or exceeds the frictional shear strength determined from the cohesion, c , normal stress, σ , and the coefficient of friction, μ , on the surface (with a compression negative sign convention):

$$|\tau| \geq c - \mu\sigma. \quad (1)$$

Opening is permitted along a fault surface when σ meets or exceeds the tensile strength along the surface, T_f :

$$\sigma \geq T_f. \quad (2)$$

Shear failure of the intact rock is permitted when $|\tau|$ meets or exceeds the frictional shear strength of the intact rock according to the Coulomb criterion and depends on the rock's inherent shear strength, S_o , and the coefficient of internal friction, μ_o :

$$|\tau| \geq S_o - \mu_o \sigma. \quad (3)$$

Opening-mode failure is permitted when σ meets or exceeds the tensile strength of the intact rock, T_o :

$$\sigma \geq T_o. \quad (4)$$

While failure can occur when and where one of these criteria is met, GROW chooses the propagation direction that optimizes the total work of the deforming system from the range of *potential growth element* angles, θ (Figure 1) [McBeck et al., 2016]. The contribution of each potential growth element to the global energy budget is evaluated as the change in external work, ΔW_{ext} , acting on the model boundaries [McBeck et al., 2016]. W_{ext} is determined from τ , σ , and the shear and normal displacements, u_s and u_n , integrated along the model boundaries, B :

$$W_{\text{ext}} = \frac{1}{2} \oint_B (\tau u_s + \sigma u_n) dB \quad (5)$$

In this study we investigate the energetics attributed to fault growth, so we calculate the change in W_{ext} associated with the addition of a growth element, which excludes the energy required for the parent fault to fail. These GROW models are run under plane strain conditions, and all elements have an out-of-plane width of 1 m and an area A_e . We present ΔW_{ext} and additional energy budget components as $\Delta \text{work}/A_e$ in units J/m².

On a potential growth element where neither the tensile nor the shear failure criterion is met, fault growth is suppressed, and $\Delta W_{\text{ext}} = 0$. W_{ext} changes with the addition of potential growth elements that fail because τ , σ , u_s , and/or u_n on the model boundaries change with such fault growth [Cooke and Madden, 2014]. This differs from the formulation presented by Griffith, 1921 and at the basis of many dynamic rupture models [e.g., Rice et al., 2005], where the durations of crack growth or earthquake rupture are much shorter than the time over which changes to the tractions and displacements occur on the model boundaries, causing the total external work to remain unchanged during coseismic deformation. GROW models explore the long-term quasi-static propagation of faults and changes to the system that produce differences in slip or opening along the faults alter the tractions and/or displacements on the model perimeters.

3. Numerical Simulations of Fault Growth

GROW captures the initial growth orientations of parent faults observed in two laboratory experiments by Bobet and Einstein [1998], one under uniaxial loading and one under biaxial loading, within experimental uncertainty. The faults under biaxial loading propagate in-line by shear failure, while faults under uniaxial loading propagate as wing cracks by tensile failure. Investigating the initial growth orientations from the tips of the parent faults under these loading conditions reveals the trade-off between propagation via tensile and shear failure.

Both laboratory experiments include two parent faults with friction of $\mu = 0.3$ embedded in rectangular blocks of gypsum with Young's modulus = 5.96 GPa and Poisson's ratio = 0.15. The faults have lengths $2a = 12.7$ mm. In the uniaxial experiment, the block is subject to loading parallel to the long sides of the gypsum block without any confining pressure ($\sigma_3 = 0$). This loading is increased incrementally until propagation initiates at $\sigma_3 = -30.4$ MPa. At this time, one fault propagates by opening-mode failure from both tips at $\theta = 124 \pm 5^\circ$, while the other fault propagates by opening-mode failure from its external tip at $\theta = 124.8 \pm 5^\circ$ [Bobet, 1997, Table 2.4]. In the biaxial experiment, the block is subject to a constant confining pressure of $\sigma_1 = -2.5$ MPa and propagation initiates when $\sigma_3 = -29$ MPa. One fault propagates in-line from its internal tip at $\theta = 180 \pm 5^\circ$ [Bobet, 1997, Table 4.2].

Figure 2a shows the GROW model used to simulate the laboratory experiments. The inherent shear strength of the material, S_o , is not provided by Bobet and Einstein [1998], but we estimate this value in simulations of the onset of failure using equation (3), $\mu_o = 0.3$ [Bobet and Einstein, 1998], and τ and σ on an element oriented at $\theta = 180^\circ$ from the external tip of one fault, prior to that element's failure, but after slip along the parent

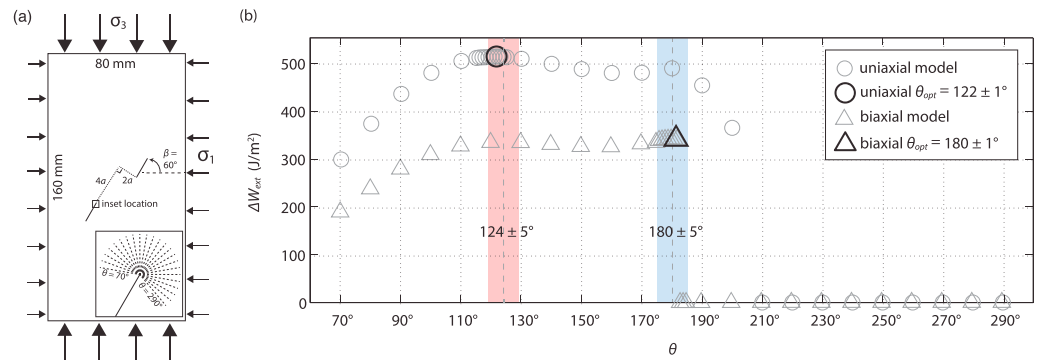


Figure 2. (a) GROW model setup. Inset shows range of potential growth elements. (b) ΔW_{ext} for all potential growth elements at one internal fault tip at the onset of fault propagation. Dashed vertical lines and colored bars indicate observation and error, respectively, from laboratory experiments.

faults. We find $S_o = 78.7$ MPa and incorporate this value into the GROW models. For the inherent tensile strength, we use $T_o = 3.2$ MPa, as reported by *Bobet and Einstein [1998]*.

3.1. Initial Propagation Directions Under Uniaxial Versus Biaxial Loading

Using GROW, we determine an initial estimate of the optimal orientation of fault propagation, θ_{opt} , by evaluating potential growth elements at 10° increments between $\theta = 70^\circ$ and 290° (Figure 2a) then refine the search at 1° increments around the initial estimate. To highlight how the energy of these two systems varies for each direction of potential fault growth, Figure 2b shows ΔW_{ext} for the potential growth elements tested at one internal fault tip in the uniaxial and biaxial models. In both the uniaxial and biaxial models, ΔW_{ext} has two local maxima at 125° and 180° . These two local maxima reveal the optimal orientations of tensile and shear failure of the potential growth elements, but only one failure mode has the largest ΔW_{ext} and is selected as θ_{opt} .

θ_{opt} matches the fault propagation orientations in the two laboratory experiments within the $\pm 5^\circ$ error reported by *Bobet and Einstein [1998]*. All four fault tips propagated in each of the GROW models, but in slightly different orientations. θ_{opt} varies from 121° to 123° in the uniaxial model and from 179° to 181° in the biaxial model. In the uniaxial GROW model, the top fault grows at $\theta_{\text{opt}} = 123^\circ$ from its external tip and at $\theta_{\text{opt}} = 122^\circ$ from its internal tip and the bottom fault grows at $\theta_{\text{opt}} = 121^\circ$ from both tips. In the biaxial GROW model, the top fault grows at $\theta_{\text{opt}} = 181^\circ$ from its external tip and at $\theta_{\text{opt}} = 179^\circ$ from its internal tip, while the bottom fault grows at $\theta_{\text{opt}} = 180^\circ$ from both tips. It is unclear whether this small variation in growth angle is a result of the models, such as the 1° search increment assigned or the asymmetry resulting from growing faults sequentially, or whether it is a variation that could be observed in laboratory experiments with a higher spatial resolution. Comparison with the experiments cannot provide information on the latter, as the resolution of the laboratory growth angles is $\pm 5^\circ$. Given these results, we assign an uncertainty of $\pm 1^\circ$ to GROW's prediction of growth direction (Figure 2b).

One difference between the biaxial GROW model and the biaxial laboratory experiment is that propagation occurs at every fault tip in the GROW model while at only one tip in the biaxial laboratory experiment. This may be due to experimental effects, for example, the production of a sharper tip at one fault end that promotes growth versus a blunter tip at the other fault end that suppresses growth. This also may be explained by phenomena not captured in the GROW models, such as spatial variations in the strength of the gypsum or the effects of propagation rate. For example, there may be local variations in the material properties of the gypsum blocks that affect fault slip and growth, giving preference for propagation at one fault tip over the other. Such heterogeneities are not explicitly incorporated in the current GROW models, but we can evaluate the effects of heterogeneities by determining the range of growth angles that produce changes in W_{ext} within 2% of θ_{opt} , creating a propagation envelop. We do so when we consider the fault growth trajectories.

3.2. Comparison of Initial Propagation Direction With Alternative Criteria

We compare the initial fault growth orientations predicted by GROW under uniaxial and biaxial loading with those determined by alternative failure criteria. For the development of a wing crack at the fault tip,

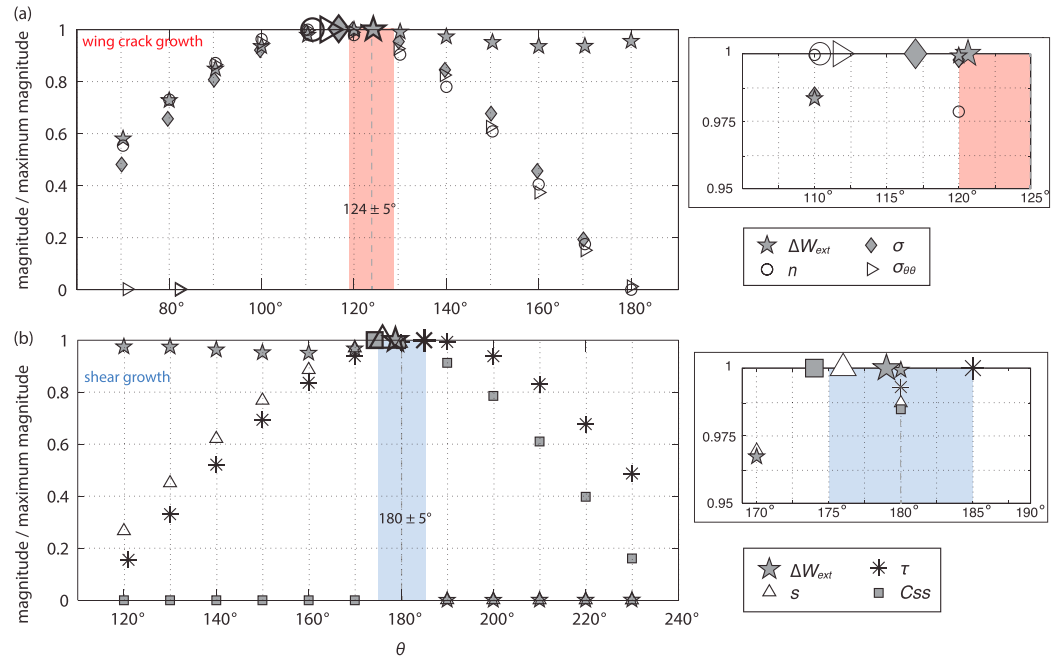


Figure 3. Comparison of GROW results with those for alternative growth criteria for models in Figure 2 with (a) uniaxial and (b) biaxial loading. The largest icons show final growth angles determined by each criterion with a refined local search at 1° increments. Insets to right zoom to region with final values. Dashed vertical line and red and blue bars indicate growth orientation with error from laboratory experiments by *Bobet and Einstein [1998]*.

alternatives include maximum normal stress, σ , maximum opening, n [e.g., *DeBremaecker and Ferris, 2004*], and maximum circumferential stress, $\sigma_{\theta\theta}$ [e.g., *Erdogan and Sih, 1963; Thomas and Pollard, 1993*]. Alternative criteria for shear failure include maximum slip, s [e.g., *DeBremaecker and Ferris, 2004*], maximum Coulomb shear stress, C_{ss} [e.g., *Anderson, 1905; Pollard and Fletcher, 2005*], and maximum shear stress magnitude, $|\tau|$ [*Wallace, 1951; Bott, 1959; Michael, 1984*].

We calculate these as follows. Slip and opening, s and n , for all potential growth orientations are reported by the numerical models. Prefailure tractions along each potential growth element are used for σ and to calculate C_{ss} , after rearranging (3) and using $T_o = S_o = 0$ and $\mu_o = 0.3$:

$$C_{ss} = |\tau| + \mu_o \sigma \quad \sigma \leq 0. \quad (6)$$

This calculation honors that the Coulomb failure criterion only is valid when tensile failure is suppressed. The relative magnitudes of $\sigma_{\theta\theta}$ with anticlockwise position from out ahead of the fault tip, Θ , are calculated at distance, r , from the fault tip, equal to half the fault element length:

$$\sigma_{\theta\theta} = \frac{1}{\sqrt{2\pi r}} \cos \frac{\Theta}{2} \left[k_I \cos^2 \frac{\Theta}{2} - k_{II} \frac{-3}{2} \sin \Theta \right] \quad (7)$$

k_I and k_{II} are the stress intensity factors for mode I and II failure, respectively [*Erdogan and Sih, 1963; Pollard and Fletcher, 2005*]. These are calculated using the numerical approximation by *Olson [1991]* and included in *Thomas and Pollard [1993, equation (5)]*.

We evaluate results for all orientations at 10° increments between $\theta = 70^\circ$ and 290° and show subsets of these results in Figure 3. To determine the growth direction, the search is then refined at 1° increments around the initial estimate value for each criterion. The final results are summarized in Table 1. We do not evaluate whether the strength of gypsum is met for each growth criterion.

All of the criteria predict fracture propagation within 25° of the laboratory observations (Figure 3 and Table 1). For uniaxial loading, work optimization best predicts the laboratory observation (Figure 3a). Maximum σ returns a growth angle of 117°. Maximum $\sigma_{\theta\theta}$ and maximum n predict lower angles of 113° and 111°,

Table 1. Growth Angles Observed in Laboratory Experiments With Two Faults and in Model Simulations According to Different Growth Criteria^a

Criterion	θ_{opt} Uniaxial	θ_{opt} Biaxial
laboratory	124 ± 5°	180° ± 5°
ΔW_{ext}	122°	179°
n	111°	113°
σ	117°	118°
$\sigma_{\theta\theta}$	113°	113°
s	177°	176°
τ	185°	185°
C_{ss}	176°	174°

^aBold values are within error of the laboratory observations.

respectively. For biaxial loading, growth by work optimization again predicts a fault growth orientation closest to the laboratory observation (Figure 3b). Maximum s and C_{ss} predict similar growth orientations at 176° and 174°, respectively, while maximum $|\tau|$ predicts growth at $\theta_{\text{opt}} = 185^\circ$.

These results show that work optimization performs as well as or better than alternative criteria for the modeled system. For growth in shear, work optimi-

zation and the maximum s and $|\tau|$ criteria all produce results within uncertainty of the laboratory observations. For growth under uniaxial loading, only work optimization produces a result within uncertainty of the laboratory growth direction. Work optimization has the advantage of evaluating growth by shear versus tensile failure, without having to select one mechanism a priori.

3.3. Propagation Paths

We also use GROW to model the propagation paths observed in two laboratory experiments by *Bobet and Einstein* [1998]. Both experiments include two underlapping faults oriented at $\beta = 60^\circ$ under biaxial loading. In one experiment, the two faults are aligned with one another (Figures 4a and 4b), while in the other, the echelon faults are offset from one another (Figures 4c and 4d). We chose these two experiments because they are representative of two classes of linkage patterns documented by *Bobet and Einstein* [1998]: Coalescence Type I—linkage by shear propagation from the fault tips and Coalescence Type II—linkage by opening-mode propagation from the fault tips. The images shown in Figures 4a and 4c are representative of these coalescence types. The intact material properties, fault properties, and loading are the same as for the models shown in Figure 2a, except that these incorporate frictionless faults that are spaced closer together in order to advance the time to fault interaction.

In the laboratory, the aligned faults propagate from their internal tips in shear and coalesce along propagation paths that are generally parallel to the parent faults (Figure 4a, Coalescence Type I from *Bobet and Einstein* [1998] (Table 3). The GROW model captures this pattern of growth (Figure 4b). Both faults initially grow in shear from their internal fault tips. First, the paths curve away from one another slightly then toward one another as they approach the initial tips of the opposite faults, to which they eventually link. In the laboratory experiment in Figure 4a, an additional switch in failure mode from shearing to opening is observed in the experiments that GROW does not capture. This may reflect a local heterogeneity that failed in tension in the laboratory experiment.

In the laboratory, the echelon faults initially propagate in-line from their internal tips and then deviate from this path to form wing cracks that link by opening-mode failure from one or both tips (Figure 4c, Coalescence Type II from *Bobet and Einstein* [1998] (Table 3). The GROW models capture this growth pattern, with propagation from both internal fault tips first in-line with the parent faults via shear failure then at an angle to the parent faults via tensile failure (Figure 4d). Eventually, each fault links to the opposite fault.

GROW captures these two coalescence patterns defined by *Bobet and Einstein* [1998]. However, the GROW propagation paths vary in certain ways from the experiments. The GROW models produce two perfectly symmetric faults, while typically, only one grows in the laboratory experiments. In addition, the experimental fault growth trajectory is more complex than that of the model faults. In the laboratory experiments, it is likely that propagation from one tip comes to dominate the system and the resulting linkage pattern, and complexity is introduced by spatial variations in the local strength of the gypsum and the relative magnitudes of stress at the two fault tips. For example, if a fault tip enters a weak region, it is able to grow faster. As that fault becomes longer relative to the other fault, it will host higher stresses at its tip, further promoting propagation, and it will come to dominate growth in the system. Alternatively, a fault tip may enter a particularly strong region in the gypsum, causing that fault to stop growing and allowing the other fault to dominate. Such strength heterogeneity is not captured by the GROW models, for which the material is homogeneous and

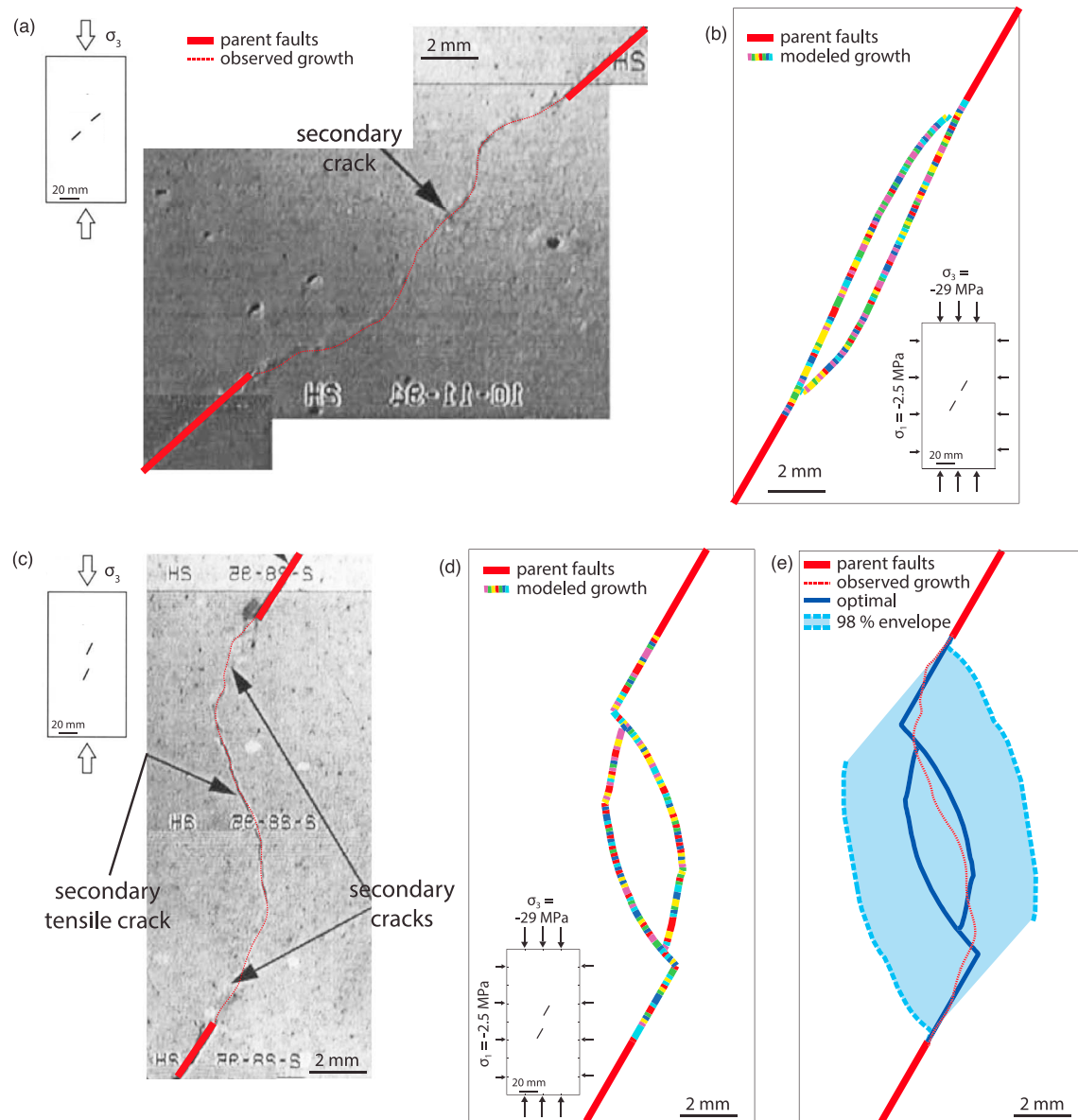


Figure 4. (a) Coalescence Type I (modified from *Bobet and Einstein* [1998, Figure 9]). *Secondary crack* indicates shear growth. Solid red lines added to highlight parent faults. Dashed red lines added to highlight growth path. (b) Fault growth in GROW following the coalescence type in Figure 4a. Colors are randomly assigned to discrete fault growth elements. (c) Coalescence Type II (modified from *Bobet and Einstein* [1998, Figure 10]). *Secondary tensile crack* indicates opening mode propagation. Solid red lines added to highlight parent faults. Dashed red lines added to highlight growth path. (d) Fault growth in GROW following coalescence type in Figure 4c. Colors are as in Figure 4b. (e) Light blue lines are the maximum limits to the 98% propagation forecast envelope. These are the fault growth paths if the maximum growth element angle that yields 98% of the ΔW_{ext} produced by the optimal growth orientation is chosen by the faults at each increment of growth. The shaded region includes all possible paths resulting from growth through a heterogeneous material.

the algorithm is designed to have growth that alternates between fault tips via the addition of elements of a constant size, resulting in perfectly symmetric growth patterns and a constant rate of simulated growth for each propagation fault.

To capture the range of growth trajectories that could result from heterogeneities in the material, Figure 5e shows the outer limits of the 98% GROW propagation forecast envelope. The forecast envelope is bounded by the propagation paths of the faults that yield 98% of the ΔW_{ext} produced by the optimal growth orientation at each growth increment. Thus, the envelope spans the locations of highly efficient potential paths that may result from growth through a medium with small heterogeneities.

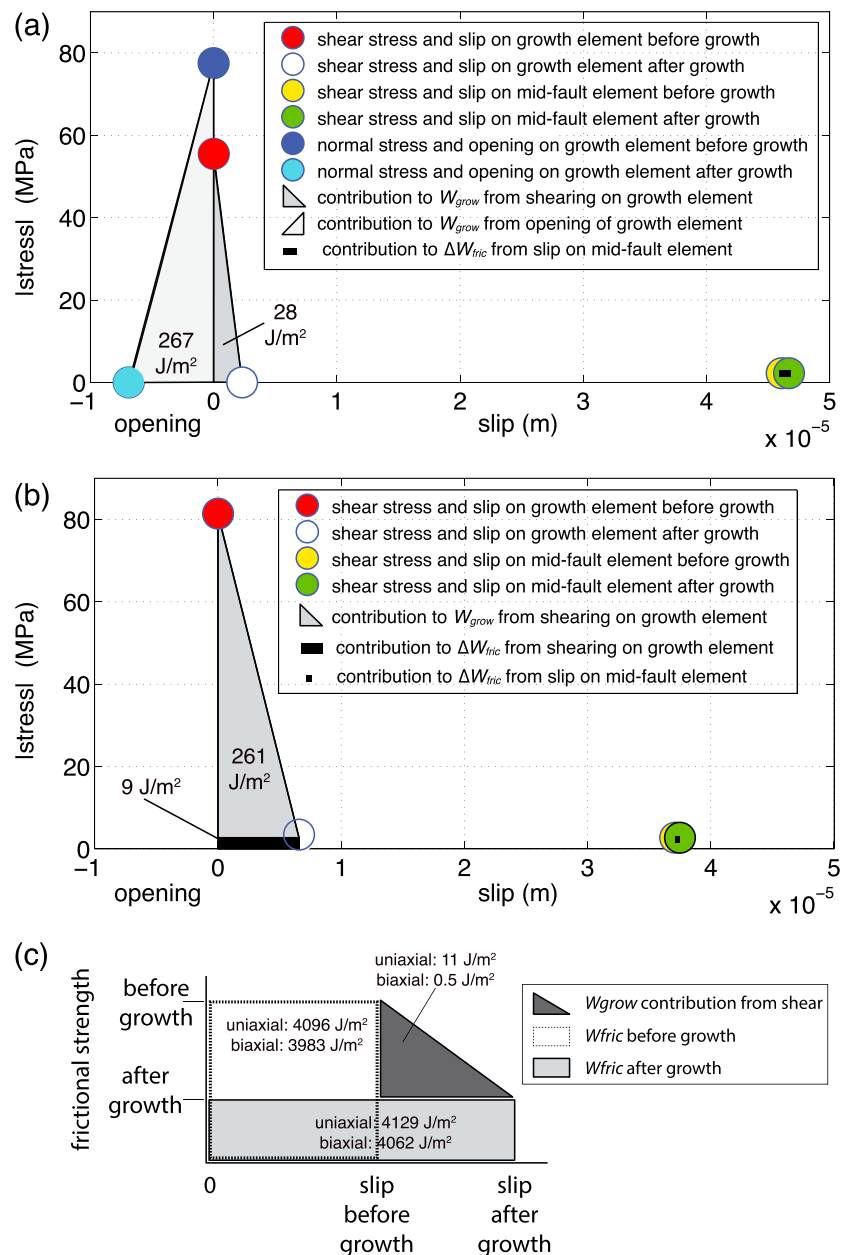


Figure 5. Stress-displacement plots showing that most W_{grow} is from shearing and/or opening of a growth element, not slip on a midfault element, for (a) the uniaxial system in Figure 2 and (b) the biaxial system in Figure 2. In Figures 5a and 5b, displacement is on the x axis and is positive for shearing and negative for opening. Absolute stress is on the y axis. The stress drop is the change in absolute stress on an element from before to after growth. The areas of the gray triangles represent W_{grow} . Slip along the midfault elements contribute to ΔW_{fric} but not to W_{grow} . (c) Plot shows the very small contribution to W_{grow} and ΔW_{fric} of additional slip along the parent fault following fault growth (not to scale). ΔW_{fric} is calculated from before to after growth.

The GROW results also raise an interesting question about the timing of fault propagation: does all failure in natural rock that can occur begin at the same moment and proceed at the same rate, or does failure at the tip of either longer faults or faults growing in weaker material occur more quickly and therefore outpace the propagation of other fractures? As noted by Bizzarri [2013], the speed of an earthquake affects the energy flux at the rupture tip and thus fault propagation as well. GROW cannot include a propagation rate explicitly but could be modified to favor growth at one fault tip over another due to some additional criterion.

4. Modeled Fault Energy Budgets

4.1. Energy Budget Terms

From these numerical experiments, we are able to calculate the complete fault energy budgets during propagation. In order to consider the complete work budget, we analyze the frictional faults shown in Figure 2. The energy budget components due to fault growth include ΔW_{int} , the change in internal work created by straining of the model material, and ΔW_{fric} , the change in energy expended during sliding at the fault's frictional strength. We also calculate W_{grow} , the energy spent to break the material to propagate a fault. W_{grow} is zero before growth, so its change is equal to its magnitude after growth. We underscore that the changes in the energy components focused on here reflect the contribution of fault growth to the energy budget and do not report the energy required to develop the parent fault. Additionally, we do not include seismic waves or slip weakening in these models, so the radiated energy is zero. We assume that the work budget components evolve linearly over the loading path, as GROW only examines the impact of new fault elements and does not capture processes during deformation or the complete paths of the energy components during growth.

W_{int} is calculated as the integral of the strain energy density, which is the product of the stress and strain tensors, σ_{ij} and ϵ_{ij} , integrated over the model volume, V [e.g., Timoshenko and Goodier, 1951; Jaeger et al., 2007]:

$$W_{\text{int}} = \iiint_V \frac{1}{2} \sigma_{ij} \epsilon_{ij} dV \quad (8)$$

W_{fric} is calculated from the shear stress, τ , and the slip, s , integrated over the modeled fault area, A :

$$W_{\text{fric}} = \iint_A \frac{1}{2} \tau s dA \quad (9)$$

The change in W_{ext} from before to after growth is balanced by commensurate changes in W_{int} and W_{fric} from before to after growth:

$$\Delta W_{\text{ext}} = \Delta W_{\text{fric}} + \Delta W_{\text{int}}. \quad (10)$$

While W_{fric} is irreversible as heat is lost to the system, W_{int} is reversible, so this energy can be stored and released and ΔW_{int} represents the energy available for other processes. W_{int} is sensitive to the discretization of the grid points used to collect the stress and strain data, so we avoid directly determining ΔW_{int} from (8) before and after growth and instead calculate ΔW_{int} by rearranging (10) following Cooke and Madden [2014].

W_{grow} is the energy consumed by fault propagation, which includes the failure of the growth element(s) and any reduction of fault strength along the parent fault that is associated with the growth of the fault. Growth may be due to shear or tensile failure. W_{grow} is the sum of the product of the change in slip, Δs , and the shear stress drop, $\Delta \tau$, and the product of the change in opening, Δn , and the normal stress drop, $\Delta \sigma$, both integrated over A :

$$W_{\text{grow}} = \Delta W_{\text{grow}} = \frac{1}{2} \iint_A \Delta \tau \Delta s dA + \frac{1}{2} \iint_A \Delta \sigma \Delta n dA \quad (11)$$

Figure 5 shows contributions to the system energy budgets for the models shown in Figure 2: one uniaxial model with $\sigma_3 = -30.4$ MPa and $\sigma_1 = 0$ and one biaxial model with $\sigma_3 = -29.0$ MPa and $\sigma_1 = -2.5$ MPa. One increment of propagation from one fault tip is considered. Figure 5a shows the energy budget for faults under uniaxial loading with wing crack formation. The majority of W_{grow} (267 J/m²) is due to the opening of the growth element, though slip along the growth element also has a small contribution (28 J/m²). Within crustal systems, tensile failure may dominate the early failure process followed by sliding of the open surface. In GROW, we cannot differentiate the timing of opening versus slip along the growth element, so we include both contributions to W_{grow} , though we note that the shear traction along the growth element is not large enough to cause shear failure. Total W_{grow} along the growth element is 284 J/m². As shown in Figure 5c, an additional 11 J/m² is contributed to W_{grow} by the increase in slip along the parent fault facilitated by fault growth. All elements along the fault contribute to ΔW_{fric} , which sums to 33 J/m². Positive contributions increase toward the growing fault tip. However, very near the crack tip, the opening of the wing crack decreases the normal stress on the parent fault and ΔW_{fric} is negative.

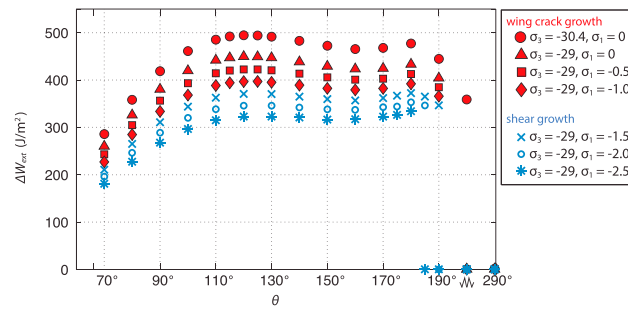


Figure 6. GROW results showing ΔW_{ext} for models with increasing confining pressure magnitude, $|\sigma_1|$, which promotes collinear fault propagation. The transition from opening-mode growth (red) with $\theta_{\text{opt}} = 120^\circ$ – 125° to shear crack growth (blue) with $\theta_{\text{opt}} = 180^\circ$ occurs when $\sigma_1 = -1.5$ MPa. $\Delta W_{\text{ext}} = 0$ where potential growth elements do not fail.

Figure 5b shows the energy budget for shear growth in-line with the parent fault. The magnitude of W_{grow} overall is similar to the uniaxial case (261 J/m^2). In this propagation scenario, there is no opening and therefore no contribution to W_{grow} from tensile failure. There also is negligible contribution to W_{grow} from additional slip along the parent fault. The 9 J/m^2 of ΔW_{fric} is associated with slip on the growth element at its frictional strength, while 70 J/m^2 of ΔW_{fric} is due to increased slip along the parent fault. The per element contribution to ΔW_{fric} is largest near the growing fault tip.

Figure 5c shows the contributions of slip along the parent faults to W_{fric} and W_{grow} . This figure is drawn schematically, because the changes from before to after growth are very small and would not be visible if it was drawn to scale. W_{fric} includes contributions from slip and stress drop due to failure of the parent fault, while ΔW_{fric} includes contributions from changes in slip and stress drop along the parent fault due to failure of the new growth element. The majority of W_{grow} for both the uniaxial and biaxial systems is due to the opening or shear of the new growth element, as can be seen from comparing W_{grow} in Figure 5c with that in Figures 5a and 5b.

The models presented here do not consider slip weakening, which can describe a nonlinear decrease in shear stress within slip. In this case, W_{grow} would be divided into W_{prop} , the energy of propagation, and W_{seis} , the energy that is lost to the system as seismic waves [Cooke and Madden, 2014]. Both are determined as in (11), but W_{prop} is calculated for $\Delta s < L$, while W_{seis} is calculated for $\Delta s > L$.

4.2. Effects of Loading and Growth Orientation on the Work Budget and Implications for Nonplanar Faults

We explore how the orientation of propagation and the resulting work budget change with one aspect of loading by running a suite of models with varying confining pressure and constant axial compression. Figure 6 shows ΔW_{ext} due to the addition of potential growth elements with orientations from 70° to 290° for a series of models. These models are configured as in Figure 2a with $\sigma_3 = -29$ MPa then with a range of confining pressures from $\sigma_1 = 0$ to -2.5 MPa. These models capture the transition at $\sigma_1 = -1.5$ MPa from fault propagation in shear parallel to the parent faults to opening-mode growth at an angle to the parent faults to form wing cracks. For this model setup, confining pressures more compressive than -1.5 MPa promote shear failure and confining pressures less compressive than this threshold promote wing cracks.

Investigating the individual work components of these models shows the trade-offs of different energetics as failure transitions from shear to tension. ΔW_{ext} decreases with increasing confining compression, because this increases the effective stiffness of these systems (Figure 7a and Table 2). ΔW_{fric} is smaller for wing crack development, because faults with opening-mode growth do not have to overcome as much frictional resistance along the potential growth element and parent fault. Correspondingly, ΔW_{int} is larger for these systems relative to those with shear growth. We find that while $\Delta W_{\text{int}} = W_{\text{grow}}$ for shear growth, $\Delta W_{\text{int}} > W_{\text{grow}}$ in systems with opening-mode growth. In addition, for both modes of growth, stress drop and slip decrease as confining pressure increases, so W_{grow} on the growth element decreases as confining pressure increases (Figure 7b).

In order to isolate the effect of fault growth orientation on the work budget, we maintain constant loading and assign the growth orientation in another suite of models run with Fric2D. For this, we use loading of $\sigma_1 = -1$ MPa and $\sigma_3 = -29$ MPa, as in the middle model in Figure 7a, near the transition between fault propagation by tensile or shear failure. Instead of automating the search for the optimal fault

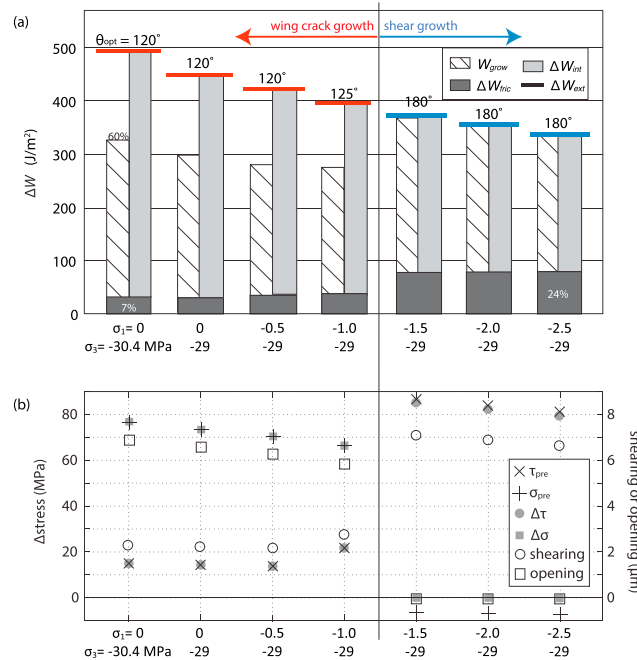


Figure 7. (a) Work budget components for the models shown in Figure 6. The x axis labels are shared by Figures 7a and 7b and indicate loading, with confining pressure, σ_1 , increasing in magnitude from left to right. (b) Stress drop (left axis) and slip or opening (right axis) on the growth elements for each model in Figure 7a. The W_{grow} magnitudes shown in Figure 7a vary with the slip and opening plotted in Figure 7b, as failure of the growth element constitutes most of W_{grow} (see Figure 5). Increasing confining pressure reduces stress drop, shearing and opening, which decreases W_{grow} .

resolved on the incipient fault plane decreases, as does the subsequent stress drop associated with failure along the new fault, thus decreasing W_{grow} [Herbert *et al.*, 2015]. We run a slightly different experiment with the GROW models, keeping maximum loading, σ_3 , constant and increasing the magnitude of the confining pressure, σ_1 (Figure 7, left to right). On a potential wing crack growth element, the magnitude of the normal stress before failure, σ_{pre} , and the normal stress drop, $\Delta\sigma$, decrease. W_{grow} decreases as well. On a potential shear growth element, σ_{pre} remains constant, but the magnitude of the shear stress before failure, τ_{pre} , and the shear stress drop, $\Delta\tau$, decrease. W_{grow} decreases as well. Given equation (11), it is not surprising that W_{grow} scales with stress drop for both modes of growth, but these models show that an increase in confining pressure can decrease the strength of the intact rock, with lower shear stresses accumulating prior to failure. This is due to a decrease in the differential stress on the incipient fault element, which controls the shear stress. In changing only confining pressure, we have isolated the effect of the shear stress on W_{grow} .

orientation with GROW, we manually add growth elements at $\theta = 100^\circ$, 120° , 140° , 160° , and 180° and compare work budget components for these scenarios (Figure 8 and Table 3). ΔW_{ext} and ΔW_{int} are similar for each of these five models, particularly from $\theta = 120^\circ$ to 180° . W_{grow} is smaller than ΔW_{int} and increases with θ until $\Delta W_{int} = W_{grow}$ at $\theta = 180^\circ$. These models also show that $\Delta W_{int} > W_{grow}$ when opening-mode growth occurs but not when shear growth occurs. This suggests that slip along a fault results in stress magnitudes at the fault tip that are exactly those required for propagation by shear failure in-line with the parent fault but larger than those required for propagation by tensional failure of a wing crack.

5. Discussion

5.1. W_{grow} and Stress Drop

Accretion experiments using dry sand analyzed by Herbert *et al.* [2015] suggest that W_{grow} scales with normal stress, which changes with the thickness of the sandpack. In experiments with successively thinner sandpacks, the magnitude of the normal compression

Table 2. Work Budget Components for the Models in Figure 7a in J/m^{2a}

σ_3	σ_1	θ_{opt}	ΔW_{ext}	ΔW_{fric}	ΔW_{int}	W_{grow}
-30.4	0.0	120	494.4	33.3	461.1	294.8
-29.0	0.0	120	449.7	30.3	419.4	268.4
-29.0	-0.5	120	422.4	35.1	387.4	247.5
-29.0	-1.0	125	397.0	38.1	359.0	235.1
-29.0	-1.5	180	372.4	78.1	294.4	300.4
-29.0	-2.0	180	353.1	78.9	274.2	280.2
-29.0	-2.5	180	334.2	79.5	254.8	260.4

^aLoading tractions are in megapascal.

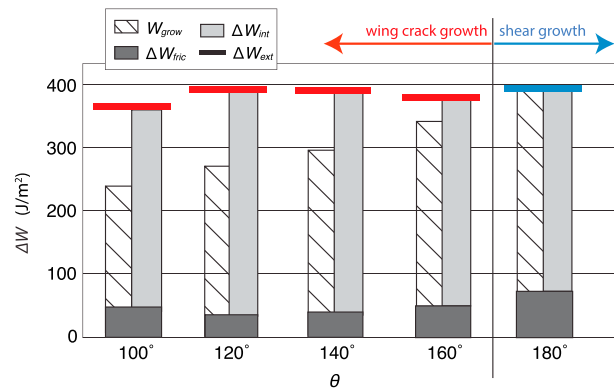


Figure 8. Models with constant loading and growth elements added at the orientations shown on the x axis. Although most work terms do not vary greatly between models, W_{grow} increases through the transition from opening-mode propagation at an angle to the parent fault to shear propagation parallel to the parent fault.

5.2. W_{grow} , G_C , and G

To understand how the experiments presented here relate to deformation at the crustal scale, we explore similarities between estimates of W_{grow} and G_C , the critical energy release rate used to explain fracture propagation under mixed-mode loading [Erdogan and Sih, 1963; Cotterell and Rice, 1980; Olson and Pollard, 1991; Lawn, 1993]. This has been adapted to studies of fault mechanics and earthquakes, in which the fracture energy, G , provides the energy available to sustain rupture [e.g., Palmer and Rice, 1973; Rice, 1980; Wong, 1982]. W_{grow} magnitudes presented here are on the order of 10^2 J/m² from models with stresses on the order

of 10^0 – 10^1 MPa ($\sigma_3 = -30$ MPa and $\sigma_1 = 0$ – 2.5 MPa). Laboratory experiments on granite blocks find that G_C ranges from 1.3 to 5.5×10^4 J/m² for maximum loading and confining pressure on the order of 10^2 MPa [Wong, 1982]. Experiments by Lockner *et al.* [1992] also use maximum loading and a confining pressure on the order of 10^2 MPa and find that G_C is $\sim 1.3 \times 10^4$ J/m² for granite and $\sim 0.25 \times 10^4$ J/m² for sandstone. A difference in the estimates of G_C in the lab experiments with those for W_{grow} of 2 orders of magnitude is consistent with a difference in loading of 2 orders of magnitude, underscoring agreement between W_{grow} and G_C .

For earthquakes, Rice *et al.* [2005] find G to be on the order of 10^6 J/m², using a formulation based on the stress drop from a dynamic slip-pulse model and seismic data for several large events by Heaton [1990]. This formulation aligns with the relationship between stress drop and W_{grow} highlighted by the models presented here. An increase in earthquake stress drop with depth has been observed in a detailed study of a high-quality catalogs [Baltay, 2014]. Hardebeck and Aron [2009] also show that earthquakes along the Hayward Fault in California, USA, have average stress drops of ~ 5 MPa up to 7 km depth, of ~ 10 MPa from 7 to 13 km depth, and of ~ 50 MPa below 13 km. Therefore, W_{grow} and G should increase with earthquake depth as well. However, we note that depth affects both confining pressure and tectonic loading. As shown by Figure 7, changing confining pressure alone can cause changes to normal and/or shear stresses, depending on the potential growth element orientation and mode of growth. Both types of stress can affect stress drop, potentially in contradictory way. This may be a reason that a dependence of stress drop on depth is difficult to discern for many groups of earthquakes and suggests that observing a depth dependence of W_{grow} and G may be difficult.

5.3. Energy Budget Scaling

While we have shown that W_{grow} is theoretically similar to G for earthquakes, the rest of the energy budget differs, because we focus on the energy associated with growth only and not slip from initial state along the parent faults plus growth. For earthquake slip, G is estimated to represent a small portion of the total energy budget, while the largest portion is taken up by frictional work [e.g., Chester *et al.*, 2005; Fulton and Rathbun, 2011]. In certain analyses, this small contribution results from defining G only in terms of the specific energy of the fault surface being considered [e.g., Fulton and Rathbun, 2011] and not considering the frictional

Table 3. Work Budget Components for the Models in Figure 8 in J/m²

θ	ΔW_{ext}	ΔW_{fric}	ΔW_{int}	W_{grow}
100°	367.9	48.2	319.7	194.1
120°	396.4	39.4	357.0	227.5
140°	388.9	38.6	350.3	257.3
160°	378.8	51.3	327.6	291.3
180°	391.8	77.0	314.8	321.4

fracture energy or damage zone energy as outlined by Xia [2006]. In a detailed analysis of failure processes that differentiates microscale and mesoscale slip behavior, Cocco and Tinti [2008] find that the “breakdown work,” which can be considered the seismological G as defined by Abercrombie and Rice [2005], forms a large part of the energy budget under certain conditions. Despite these considerations, the definitions of the energy budget terms used here are restricted only to processes related to fault propagation and W_{grow} represents the majority of the energy budget. It is 60% of the work budget for tensile growth of a wing crack at an angle to the parent fault and 76% for growth in shear in-line with the parent fault (Figure 7) for the models presented here, while only 7% and 24% of the total energy is taken up by frictional heating in the two models, respectively. Any additional slip along the parent fault due to fault propagation is included in ΔW_{fric} , but we do not analyze the total frictional work required to slip the parent fault initially, which can be much larger than ΔW_{fric} (Figure 5c). This is why W_{grow} represents a large part of these energy budgets.

5.4. Excess Energy From Kinked Growth

Figures 7a and 8 show that $\Delta W_{\text{int}} > W_{\text{grow}}$ when opening-mode growth occurs at an angle to the parent fault but not when shear growth in-line with the parent fault occurs. Thus, slip results in stress magnitudes at the fault tip that are exactly those required for shear growth but larger than those required for wing crack growth. In the Earth, propagation at an angle to the parent fault, either at a fault tip or along a fault, may involve significant plastic deformation due to high strains at the resulting kink. This would mean that some portion of the excess ΔW_{int} would be absorbed into permanent deformation [e.g., Shipton *et al.*, 2006]. This may be similar to the damage zone energy outlined by Wong [1982] and Xia [2006]. This energy also may be available for other processes, such as the acceleration of propagation and/or the production of seismic waves, which are observed as acoustic emissions in many laboratory experiments [e.g., Lockner *et al.*, 1991]. In this case, some of the excess ΔW_{int} could be expressed as W_{seis} . At the kilometer scale, this means that nonplanar fault slip and propagation may provide energy for additional deformation and seismic activity, including the development of off-fault damage, aftershock occurrence, and rupture acceleration.

6. Conclusions

We present models for which fault growth is consistent with system evolution toward higher efficiency. Using this global work criterion allows for growth by a different mode of failure for each increment of propagation and shows that growth by opening-mode or shear failure results in distinct energy budgets. W_{grow} is 76% of the energy budget of a fault propagating within intact rock by shearing, in-line with the parent fault. The internal strain energy produced is equal to that required for shear propagation. ΔW_{fric} is 24% of the energy budget. For wing crack growth, W_{grow} and ΔW_{fric} are 60% and 6%, respectively. However, the internal strain energy produced for opening-mode propagation is in excess of that required ($W_{\text{grow}} < \Delta W_{\text{int}}$), suggesting that nonplanar propagation provides energy for other processes. We note that these results reflect propagation in perfectly homogeneous materials, while propagation through a heterogeneous medium could result in the range of growth paths bounded by the 98% propagation forecast. A comparison of W_{grow} and the critical energy release rate, G_C , determined from laboratory experiments shows that the magnitudes produced here scale with G_C . In addition, we demonstrate that the stress drop dependence of W_{grow} is consistent with that of the fracture energy, G , for earthquakes but highlight that any depth dependence of stress drop, W_{grow} , and G may be hard to observe due to variations in confining pressure and loading both laterally and with depth, which can cause potentially opposing changes in shear stress, normal stress, and stress drop on an incipient fault.

Appendix A

A1. Element Length Along the Model Faults

The element length along the faults, e , controls the length of the potential growth elements. The potential growth element length must be short enough to capture the concentrated stress field near the fault tip but long enough to exceed the plastic or microcracking zone at the fault tip, where stresses in linear elastic materials approach infinity and exceed the yield stress of the material [Whittaker *et al.*, 1992]. In order to evaluate whether e is short enough to capture the near-tip stress field, we test that two criteria are met:

(1) that the modeled growth orientation corresponds to the analytical solution for the orientation of 108° of the maximum circumferential stress at the tip of a mode II fault [Lawn, 1993, p. 25] and (2) that this angle is independent of β , the orientation of the fault clockwise from σ_3 . These conditions have been explored in other numerical models. Using the maximum mode I stress intensity factor to determine the growth orientation, Nemat-Nasser and Horii [1982, Figures 4–6] show that both conditions are met when $e/a = 0.01$, where $2a$ is fault length but that the growth orientation increases and becomes dependent on β as e/a increases. Using maximum opening as the growth criterion, DeBremaecker and Ferris [2004, p. 2166] find a growth orientation of $110^\circ \pm 3^\circ$ that is independent of β when $e/a \leq 0.02$ but that varies with β when $e/a \sim 0.10$.

We compare six GROW models that each include a single fault with $e/a = 0.02$ in a gypsum block subject to uniaxial loading of $\sigma_3 = -30.4$ MPa. β varies between models by 10° increments from 20° to 70° . First, we search for the orientation of maximum opening at 10° increments between $\theta = 70^\circ$ and 290° , then we refine the search at 1° increments around the initial estimate. We find that the average orientation of maximum opening across all models is $110^\circ \pm 3.2^\circ$. These results are consistent with the analytical solution by Lawn [1993], and the results of DeBremaecker and Ferris [2004] and confirm that $e/a = 0.02$ ($e = 0.127$ mm) is short enough to capture the near-tip stress field. In addition, we find that the condition number for each model, normalized by the number of elements in that model, does not vary with e . It remains constant at $6.5172e^7/\text{element}$.

In order to evaluate whether $e/a = 0.02$ ($e = 0.127$ mm) is long enough to extend beyond the near-tip plastic zone, we confirm that this length exceeds the radius of this zone, r . This is generally considered to be a material property associated with yield strength [e.g., Woo and Ling, 1984]. In addition, we note that the stresses at a distance of $r = e = 0.127$ mm from the fault tip are finite, indicating that we are sampling beyond the plastic zone. For example, the stresses on the growth element oriented at 110° at the tip of a fault with $\beta = 60^\circ$ are $\sigma_n = 77.1$ MPa and $|\sigma_s| = 15.1$ MPa. GROW does not account for any plastic deformation within this zone that could occur and alter the conditions on the potential growth elements.

A2. Element Length Along the Model Perimeters

The length of the elements along a GROW model's perimeters, e_p , also must be considered. Having equal length for all elements in a model (e.g., along both faults and perimeters) provides the most robust matrix inversion for the boundary element method [Crouch and Starfield, 1983]. However, allowing for longer elements along the boundaries significantly reduces the computation time. We evaluate if $e_p > e$ is permissible, such that the orientation and magnitude of the potential growth element with maximum opening remains unaffected.

We compare five GROW models that each include a single fault with $e/a = 0.02$ and $\beta = 60^\circ$ in a gypsum block subject to uniaxial loading of $\sigma_3 = -30.4$ MPa. Each model has a different boundary element length of $e_p = 2$ mm, 1 mm, 0.500 mm, 0.250 mm, and 0.127 mm. Note that when $e_p = 0.127$ mm, $e_p = e$. First, we search for the orientation of maximum opening at 10° increments between $\theta = 70^\circ$ and 290° , then we refine the search at 1° increments around the initial estimate. We find that for all of these models, maximum opening occurs on the potential growth element oriented at 111° . In addition, the magnitudes of maximum opening exhibit low dependence on e_p , averaging $7.1e^{-06} \pm 4.2e^{-08}$ mm. In addition, W_{ext} prior to growth shows a low dependency on e_p , averaging 989.1 ± 8.9 J across all five models. These results indicate that improving computational efficiency by including longer elements on the perimeter of the model does not compromise the results and use $e_p = 1$ mm in all models. However, the condition number for each model, normalized by the number of elements in that model, does decrease as e_p decreases, from $1.0912e^8/\text{element}$ when $e_p = 2$ mm to $9.9316e^6/\text{element}$ when $e_p = 0.127$ mm.

References

- Abercrombie, R. E., and J. R. Rice (2005), Can observations of earthquake scaling constrain slip weakening?, *Geophys. J. Int.*, *162*(2), 406–424.
- Anderson, E. M. (1905), The dynamics of faulting, *Trans. Edinburgh Geol. Soc.*, *8*(3), 387–402.
- Baltay, A. S. (2014), Stress drop and its relationship to radiated energy, ground motion and uncertainty, Abstract S51C-08 presented at 2014 Fall Meeting, AGU, San Francisco, Calif., 15–19 Dec.
- Bizzarri, A. (2013), Energy flux of propagating ruptures with cohesive force, *Bull. Seismol. Bull. Am.*, *103*(5), 2670–2679.
- Bobet, A. (1997), Fracture coalescence in rock materials: Experimental observations and numerical predictions, DSc thesis, Mass. Inst. of Technol., Cambridge.

Acknowledgments

This work was made possible by the National Science Foundation under grant EAR-1219919. The data presented in this manuscript are available from E. H. Madden. The modeling tool GROW is available from github (<https://github.com/mlcooke/GROW>). Fric2D is available with documentation for download from <http://www.geo.umass.edu/faculty/cooke/software.html>. Two anonymous reviewers greatly improved this manuscript.

- Bobet, A., and H. H. Einstein (1998), Fracture coalescence in rock-like materials under uniaxial and biaxial compression, *Int. J. Rock Mech. Min. Sci.*, **35**, 863–888.
- Bott, M. (1959), The mechanics of oblique slip faulting, *Geol. Mag.*, **96**, 109–117.
- Chester, J. S., F. M. Chester, and A. K. Kronenberg (2005), Fracture surface energy of the Punchbowl fault, San Andreas system, *Nature*, **37**, 133–136.
- Cocco, M., and E. Tinti (2008), Scale dependence in the dynamics of earthquake propagation: Evidence from seismological and geological observations, *Earth Planet. Sci. Lett.*, **273**(1), 123–131.
- Cooke, M. L., and E. H. Madden (2014), Is the Earth lazy? A review of work minimization in fault evolution, *J. Struct. Geol.*, **66**, 334–346.
- Cooke, M. L., and S. Murphy (2004), Assessing the work budget and efficiency of fault systems using mechanical models, *J. Geophys. Res.*, **109**, B10408, doi:10.1029/2004JB002968.
- Cooke, M. L., and D. D. Pollard (1997), Bedding plane slip in initial stages of fault-related folding, *J. Struct. Geol.*, **19**, 567–581.
- Cooke, M. L., F. Islam, and G. McGill (2011), Basement controls on the scale of giant polygons in Utopia Planitia, Mars, *J. Geophys. Res.*, **116**, E09003, doi:10.1029/2011JE003812.
- Cotterell, B., and J. R. Rice (1980), Slightly curved or kinked cracks, *Int. J. Fract.*, **16**(2), 155–169.
- Crider, J. G., and D. C. P. Peacock (2004), Initiation of brittle faults in the upper crust: A review of field observations, *J. Struct. Geol.*, **26**, 691–707.
- Crouch, S. L., and A. M. Starfield (1983), *Boundary Element Methods in Solid Mechanics*, George Allen and Unwin, London.
- DeBremaecker, J.-C., and M. C. Ferris (2004), Numerical models of shear fracture propagation, *Eng. Fract. Mech.*, **71**, 2161–2178.
- Del Castello, M., and M. L. Cooke (2007), Underthrusting-accretion cycle: Work budget as revealed by the boundary element method, *J. Geophys. Res.*, **112**, B12404, doi:10.1029/2007JB004997.
- Erdogan, F., and G. C. Sih (1963), On the crack extension in plates under plane loading and transverse shear, *Trans. Am. Soc. Mech. Eng.*, **85**, 519–527.
- Fulton, P. M., and A. P. Rathbun (2011), Experimental constraints on energy partitioning during stick-slip and stable sliding within analog fault gouge, *Earth Planet. Sci. Lett.*, **308**, 185–192.
- Griffith, A. A. (1921), The phenomena of rupture and flow in solids, *Philos. Trans. R. Soc. London*, **A221**, 163–198.
- Hardebeck, J. L., and A. Aron (2009), Earthquake stress drops and inferred fault strength on the Hayward Fault, East San Francisco Bay, California, *Bull. Seismol. Soc. Am.*, **99**(3), 1801–1814.
- Heaton, T. H. (1990), Evidence for and implications of self-healing pulses of slip in earthquake rupture, *Earth Planet. Int.*, **64**, 1–20.
- Herbert, J. W., M. L. Cooke, P. Souloumiac, E. H. Madden, B. C. L. Mary, and B. Maillot (2015), The work of fault growth in laboratory sandbox experiments, *Earth Planet. Sci. Lett.*, **432**, 95–102.
- Horii, H., and S. Nemat-Nasser (1985), Compression-induced microcrack growth in brittle solids: Axial splitting and shear fracture, *J. Geophys. Res.*, **90**, 3105–3125.
- Jaeger, J., N. Cook, and R. Zimmermann (2007), *Fundamentals of Rock Mechanics*, Blackwell, Malden, Mass.
- Lawn, B. (1993), *Fracture of Brittle Solids*, 2nd ed., 378 pp., Cambridge Univ. Press, Cambridge.
- Lockner, D. A., J. D. Byerlee, W. Kuksenko, A. Ponomarev, and A. Sidorin (1991), Quasi-static fault growth and shear fracture energy in granite, *Nature*, **350**, 39–42.
- Lockner, D. A., J. D. Byerlee, W. Kuksenko, A. Ponomarev, and A. Sidorin (1992), Observations of quasistatic fault growth from acoustic emissions, in *Fault Mechanics and Transport Properties of Rocks—A Festschrift in Honor of W. F. Brace*, *Int. Geophys.*, vol. 51, chap. 1, pp. 3–31, Academic Press, London.
- Lunn, R. J., J. P. Willson, Z. K. Shipton, and H. Moir (2008), Simulating brittle fault growth from linkage of preexisting structures, *J. Geophys. Res.*, **113**, B07403, doi:10.1029/2007JB005388.
- McBeck, J., E. H. Madden, and M. C. Cooke (2016), Growth by Optimization of Work (GROW): A new modeling tool that predicts fault growth through work minimization, *Comput. Geosci.*, **88**, 142–151.
- Michael, A. J. (1984), Determination of stress from slip data: Faults and folds, *J. Geophys. Res.*, **89**, 11,517–11,526, doi:10.1029/JB089iB13p11517.
- Moir, H., R. J. Lunn, Z. K. Shipton, and J. D. Kirkpatrick (2010), Simulating brittle fault evolution from networks of pre-existing joints within crystalline rock, *J. Struct. Geol.*, **32**(11), 1742–1753, doi:10.1016/j.jsg.2009.08.016.
- Nemat-Nasser, S., and H. Horii (1982), Compression-induced nonplanar crack extension with application to splitting, exfoliation, and rockburst, *J. Geophys. Res.*, **87**, 6805–6821.
- Olson, J., and D. D. Pollard (1991), The initiation and growth of en echelon veins, *J. Struct. Geol.*, **13**, 595–608.
- Olson, J. E. (1991), *Fracture Mechanics Analysis of Joints and Veins*, PhD thesis, Stanford Univ., Stanford, Calif.
- Palmer, A. C., and J. R. Rice (1973), The growth of slip surfaces in the progressive failure of over-consolidated clay, *Proc. R. Soc. London A*, **322**, 527–548.
- Petit, J. P., and M. Barquins (1988), Can natural faults propagate under mode II conditions?, *Tectonics*, **7**, 1243–1256, doi:10.1029/TC007i006p01243.
- Pollard, D. D., and R. C. Fletcher (2005), *Fundamentals of Structural Geology and Geomechanics*, Cambridge Univ. Press, New York.
- Rice, J. R. (1980), The mechanics of earthquake rupture, in *Physics of the Earth's Interior*, *Proc. International School of Physics "Enrico Fermi"*, edited by A. M. Dziewonski and E. Boschi, pp. 555–649, Italian Phys. Soc., Bologna, and North Holland Co., Amsterdam.
- Rice, J. R., C. G. Sammis, and R. Parsons (2005), Off-fault secondary failure induced by a dynamic slip pulse, *Bull. Seismol. Soc. Am.*, **95**(1), 109–134, doi:10.1785/0120030166.
- Savage, H. M., and M. L. Cooke (2010), Unlocking the effects of friction on fault damage zones, *J. Struct. Geol.*, **32**(11), 1732–1741, doi:10.1016/j.jsg.2009.08.014.
- Shipton, Z. K., J. P. Evans, R. E. Abercrombie, and E. E. Brodsky (2006), The missing sinks: Slip localization in faults, damage zones, and the seismic energy budget, in *Earthquakes: Radiated Energy and the Physics of Faulting*, *Geophys. Monogr. Ser.*, vol. 170, edited by R. Abercrombie et al., pp. 217–222, AGU, Washington, D. C.
- Thomas, A. L., and D. D. Pollard (1993), The geometry of echelon fractures in rock: Implications from laboratory and numerical experiments, *J. Struct. Geol.*, **15**, 323–334.
- Timoshenko, S. P., and J. N. Goodier (1951), *Theory of Elasticity*, 2nd ed., McGraw-Hill, New York.
- Wallace, R. (1951), Geometry of shearing stress and relation to faulting, *J. Geol.*, **59**, 118–130.
- Whittaker, B. N., R. N. Singh, and G. Sun (1992), *Rock Fracture Mechanics: Principles, Design, and Applications*, Elsevier, Amsterdam.
- Wong, T.-F. (1982), Shear fracture energy of westerly granite from post-failure behavior, *J. Geophys. Res.*, **87**, 990–1000, doi:10.1029/JB087iB02p00990.

- Woo, C. W., and L. H. Ling (1984), On angled crack initiation under biaxial loading, *J. Strain Anal. Eng.*, 19(1), 51–59.
- Xia, K. (2006), Scaling of fracture energies: The rationalization of different laboratory measurements, *Geophys. Res. Lett.*, 33, L01305, doi:10.1029/2005GL024446.
- Yagupsky, D. L., B. A. Brooks, K. X. Whipple, C. C. Duncan, and M. Bevis (2014), Distribution of active faulting along orogenic wedges: Minimum-work models and natural analogue, *J. Struct. Geol.*, 66, 237–247, doi:10.1016/j.jsg.2014.05.025.